

# Automatic Leptonic Tensor Generation for Beyond the Standard Model (BSM) Theories

---

Diego Lopez Gutierrez<sup>a</sup> Joshua Isaacson<sup>b</sup>

<sup>a</sup>*Macalester College,  
1600 Grand Avenue, Saint Paul, MN, USA*

<sup>b</sup>*Theoretical Physics Department, Fermi National Accelerator Laboratory,  
Kirk Road and Pine Street, Batavia, IL 60510*

*E-mail:* [dlopezgu@macalester.edu](mailto:dlopezgu@macalester.edu), [isaacson@fnal.gov](mailto:isaacson@fnal.gov)

**ABSTRACT:** With the development of the Deep Underground Neutrino Experiment (DUNE) and Tokai-to-Hyper-Kamiokande (T2HK), we are entering the era of high-precision neutrino measurements. The colossal output of data from DUNE, plus the current data from several other neutrino experiments, will require a fast and efficient method of testing our BSM models in event generators. However, current methods for implementing a BSM theory in the event generators are prone to errors and time consuming. We propose a novel program capable of automatically calculating the leptonic tensor for a given quantum field theory Lagrangian. This C++ program utilizes the `Universal FeynRules Output (UFO)` format, and the Berends-Giele recursive relations to produce leptonic tensors that can be automatically implemented in several neutrino event generators, including those relevant for DUNE. To compare the results of our program to the literature, we implement a multichannel Monte Carlo phase space integrator, the `VEGAS` algorithm and supply the corresponding hadronic tensors based on a collaborator's theoretical calculations. We present two SM processes,  $e^-p^+ \rightarrow e^-p^+$  and  $\nu_e p^+ \rightarrow \nu_e p^+$ , to show the promising results of a previous version of our program. These results have a computational vs. analytic ratio of about 1 and 0.9, respectively. Lastly, we also include some preliminary results of the most up-to-date version of our program that incorporates the multichannel and `VEGAS` techniques. These new results are equally as promising, validating our approach and giving us confidence that the testing of more complicated SM and BSM scenarios will yield correct results.

---

## Contents

<b>1</b>	<b>Introduction</b>	<b>1</b>
1.1	Cross Section	2
1.2	Lagrangian and Feynman Diagrams	3
1.3	Hadronic and Leptonic Tensor	5
<b>2</b>	<b>Methods</b>	<b>7</b>
2.1	Universal FeynRules Output	7
2.2	Berends-Giele Recursive Relations	8
2.3	Multichannel Monte Carlo Phase Space Integration	9
2.4	VEGAS Algorithm	12
2.5	BSM Models to UFO Files	12
<b>3</b>	<b>Results and Discussion</b>	<b>14</b>
3.1	$e^-p^+ \rightarrow e^-p^+$	14
3.2	$\nu_e p^+ \rightarrow \nu_e p^+$	18
3.3	Preliminary Results	22
<b>4</b>	<b>Conclusion and Future Steps</b>	<b>23</b>

---

## 1 Introduction

The Standard Model (SM) is our most accurate physics theory capable of describing three of the four known fundamental forces of nature along with their corresponding particles. However, the SM is an incomplete theory as it does not include gravity and it fails to explain dark matter, dark energy, and a variety of other phenomena. For example, the SM predicts that only left-handed massless neutrinos exist, contradicting experimental evidence of massive neutrinos via neutrino oscillations as reported by the Super-Kamiokande [18], SNO [8] and KamLAND [17] experiments. Since then, several experiments have found anomalies regarding the behavior of neutrino oscillations at short-baselines, hinting at the existence of a fourth type of neutrino that is sterile to any SM interactions [4–7, 16, 19, 26]. To explain the phenomena of neutrino oscillations, the origin of its mass, the existence of a possible sterile neutrino and other interesting experimental evidence, scientists develop Beyond the Standard Model (BSM) theories. However, many BSM processes are too complex to be evaluated by hand. Instead, we rely on event generators such as Genie [10], NuWro [21], NEUT [22], and GiBUU [13, 27] to obtain predictions that we can then compare to experimental data.

Within the next decade, we are entering an era of high-precision neutrino studies. The neutrino community will be enriched with colossal amounts of data coming from the

Deep Underground Neutrino Experiment (DUNE) [3] and the Tokai-to-Hyper-Kamiokande (T2HK) [1] collaborations. The unprecedented number of neutrino events coming from these two experiments, plus the data that we already have from experiments such as MicroBooNE [2], will allow for the testing of several BSM theories. However, the current method of manually implementing a BSM theory into an event generator is inadequate. The manual implementation process is prone to errors due to the different code conventions of each event generator, which inevitably lead to human errors, and is time-consuming given that the user has to repeat all the work for each BSM model. Due to these setbacks and because of the large number of theories to be tested, this current process becomes infeasible. Instead, we propose an algorithm that automates the testing process.

Event generators calculate Feynman diagram amplitudes from a set of input momenta. The squared sum of these amplitudes is closely related to experimental observables such as decay widths and cross sections. For the neutrino interactions we are considering, we can always decompose this squared sum into two quantities: the leptonic and the hadronic tensor. Any effects of BSM physics that are present in the hadronic tensor would be discovered by experiments such as the Large Hadron Collider (LHC) before being detected at DUNE or T2HK. Consequently, for DUNE and T2HK, it is most useful to focus on analyzing the leptonic tensor instead. We propose a novel program that automates the implementation of BSM theories in event generators by automatically calculating the leptonic tensor of the theory given its Lagrangian. Moreover, our algorithm can be easily interfaced to several neutrino event generators. The C++ program relies on the `Universal FeynRules Output` (UFO) file [15] and the Berends-Giele algorithm [11], and it is based on the development of the COMIX [20] matrix element generator from Sherpa [23]. Before we dive into the details of the program, let us review some particle physics and quantum field theory concepts.

## 1.1 Cross Section

To study the properties of particles and their interactions, we must rely on experimental observables, quantities that can be measured and that will tell us something about a given event. Among these observables are cross sections and decay widths, which can be measured in particle physics experiments by colliding particles with each other or analyzing their decays. In this section, we will only focus on the cross section.

The cross section ( $\sigma$ ) tells us about the effective (cross sectional) area that particle B presents to particle A when they collide. Then,  $\sigma$  is a measure of the likelihood that particles A and B collide. We can calculate  $\sigma$  following Fermi's Golden Rule for the cross section. For a process with two initial particles  $A_1, A_2$  and  $n$  final particles  $B_1, B_2, \dots, B_n$ , the cross section is given by

$$\sigma(A_1 A_2 \rightarrow B_1 B_2 \dots B_n) = \frac{S}{2\sqrt{\lambda(E_{CM}^2, m_{A_1}^2, m_{A_2}^2)}} \int d\Pi_n |\mathcal{M}|^2, \quad (1.1)$$

where  $|\mathcal{M}|^2$  is the square of the amplitude sum,  $\lambda(E_{CM}^2, m_{A_1}^2, m_{A_2}^2) = E_{CM}^4 + m_{A_1}^4 + m_{A_2}^4 - 2(E_{CM}^2 m_{A_1}^2 + m_{A_1}^2 m_{A_2}^2 + E_{CM}^2 m_{A_2}^2)$  is the Källén function with  $E_{CM}$  as the center-of-mass

energy,  $S$  is a symmetry factor and  $d\Pi_n$  is the  $n$ -dimensional phase space given by

$$\int d\Pi_n = \int (2\pi)^4 \delta^{(4)} \left( \sum_i p_{A_i} - \sum_{i=1}^n p_{B_i} \right) \prod_{j=1}^n \frac{1}{2E_{B_j}} \frac{d^3\vec{p}_{B_j}}{(2\pi)^3}. \quad (1.2)$$

As we can see from Eq. 1.1, the cross section  $\sigma$  is proportional to the integral over phase space of the squared amplitude sum,  $|\mathcal{M}|^2$ . Therefore, calculating this quantity is necessary for obtaining the aforementioned observable.

## 1.2 Lagrangian and Feynman Diagrams

The Lagrangian  $\mathcal{L}$  contains all the information about the particles and interactions of a theory. It is closely related to the action ( $\mathcal{S}$ ) and the least action principle ( $\delta\mathcal{S} = \int d^4x \delta\mathcal{L}$ ) of classical field theory. Quantum Electrodynamics (QED) is the quantum field theory that governs the electromagnetic interactions via the exchange of the photon  $\gamma$ . Before generalizing for all fermions, let us consider the Lagrangian of a universe with only photons and electrons. The QED Lagrangian for this universe would be

$$\begin{aligned} \mathcal{L}_{\text{QED}} &= -\frac{1}{4} F_{\mu\nu} F^{\mu\nu} - j^\mu A_\mu + \bar{\psi}(i\gamma^\mu \partial_\mu - m)\psi \\ &= -\frac{1}{4} F_{\mu\nu} F^{\mu\nu} + \bar{\psi}(i\gamma^\mu \partial_\mu - m)\psi - Q_e e \bar{\psi} \gamma^\mu \psi A_\mu, \end{aligned}$$

where  $F_{\mu\nu}$  is the electromagnetic field-strength tensor,  $\gamma^\mu$  are the Dirac gamma matrices obeying the anticommutation relation  $\{\gamma^\mu, \gamma^\nu\} = 2g^{\mu\nu}$ ,  $\psi$  ( $\bar{\psi}$ ) is the electron (positron) Dirac field operator,  $A_\mu$  is the photon field operator,  $e$  is the elementary charge and  $Q_e$  is the electric charge of the electron in units of  $e$  (i.e.  $Q_e = -1$ ). The term  $-Q_e e \bar{\psi} \gamma^\mu \psi A_\mu$  contains the electron ( $\psi$ ), positron ( $\bar{\psi}$ ) and photon ( $A_\mu$ ) fields and it represents the interaction between a photon and an electron/positron pair. We can generalize the QED Lagrangian for all fermions and antifermions by taking into account the different charges of the particles,

$$\mathcal{L}_{\text{QED}} = -\frac{1}{4} F_{\mu\nu} F^{\mu\nu} + \sum_{\text{all fermions}} \bar{\psi}_f (i\gamma^\mu \partial_\mu - Q_f e \gamma^\mu A_\mu - m_f) \psi_f, \quad (1.3)$$

where  $m_f$  is the fermion mass (e.g.  $m_e$  for the electron),  $Q_f$  is the fermion electric charge (e.g.  $-1$  for the electron) and  $\psi_f, \bar{\psi}_f$  are the corresponding fermion and antifermion Dirac spinors. This QED Lagrangian is the blueprint of all SM electromagnetic interactions in the universe. Let us now study Feynman diagrams.

A Feynman diagram is a pictorial representation of a term in the perturbative expansion of the total amplitude  $\mathcal{M}$  in powers of  $\alpha_{\text{EM}} = \frac{e^2}{4\pi}$ , the electromagnetic coupling constant. For simplicity, we will express our expansion in terms of powers of  $e$ . Thus, the total amplitude  $\mathcal{M}$  is expressed as

$$\mathcal{M} = \mathcal{M}_0(e^0) + \mathcal{M}_1(e^1) + \dots,$$

where each term  $\mathcal{M}_j$  in this perturbative expansion of  $\mathcal{M}$  corresponds to a spacetime process. We represent this process via a Feynman diagram. For this work, we restrict

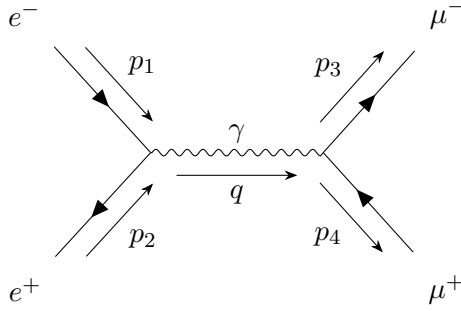


**Figure 1.** Tree-level Feynman diagram of  $e^+e^- \rightarrow \mu^+\mu^-$  for particles with 4-momenta  $p_1, p_2, p_3, p_4$ .

ourselves to tree-level (i.e. first-order) diagrams; that is, those diagrams with the lowest order in  $\alpha$  that are nonzero. An example of a Feynman diagram is given in Fig. 1 for the  $e^+e^- \rightarrow \mu^+\mu^-$  process via the exchange of a photon. A process can have more than one Feynman diagram at tree-level, in which case the Feynman diagram amplitudes are added before squaring (i.e.  $|\mathcal{M}|^2 = |\sum_i \mathcal{M}_i|^2$ .) To calculate the amplitude of a Feynman diagram, we rely on the Feynman rules. These Feynman rules are obtained from the Lagrangian; one example would be the rule for the interaction of a fermion/antifermion pair with a photon. From the QED Lagrangian, we notice that the term representing this interaction is given by  $\mathcal{L}_{\text{int}} = \sum_{\text{all fermions}} -Q_f e \bar{\psi}_f \gamma^\mu \psi_f A_\mu$ . The Feynman rule associated to this interaction term in the Lagrangian is  $iQ_f e \gamma^\mu$ . Some of the Feynman rules for QED are given below,

Initial fermion:		$= u^s(p)$
Initial antifermion:		$= \bar{v}^s(p)$
Final fermion:		$= \bar{u}^s(p)$
Final antifermion:		$= v^s(p)$
Photon propagator:		$= \frac{-ig_{\mu\nu}}{q^2}$
Photon-fermion/antifermion vertex:		$= iQ_f e \gamma^\mu$

where  $u, \bar{u}, v, \bar{v}$  are the Dirac spinors in momentum space and the second to last term is the photon propagator required for virtual photons. To obtain the amplitude from a Feynman

diagram, we simply use these rules to express the diagram in a mathematical form. The amplitude is the corresponding products of each of these factors. Let us quickly review the example from Fig. 1. For this diagram, we have an initial electron, an initial positron, a final muon, a final antimuon, a photon propagator and two photon-fermion/antifermion vertices. The amplitude for this diagram is thus given by

$$\mathcal{M} = \underbrace{\bar{v}^{s'}(p_2)}_{e^+} \underbrace{(-ie)\gamma^\mu}_{e^+e^-\gamma \text{ vertex}} \underbrace{u^s(p_1)}_{e^-} \underbrace{\frac{-ig_{\mu\nu}}{q^2}}_{\gamma} \underbrace{\bar{u}^{r'}(p_3)}_{\mu^-} \underbrace{(-ie)\gamma^\nu}_{\mu^+\mu^-\gamma \text{ vertex}} \underbrace{v^r(p_4)}_{\mu^+}. \quad (1.4)$$

### 1.3 Hadronic and Leptonic Tensor

For neutrino interactions, we can express the squared amplitude as

$$|\mathcal{M}|^2 = L_{\mu\nu} H^{\mu\nu}, \quad (1.5)$$

where  $L_{\mu\nu}$  is called the leptonic tensor and  $H^{\mu\nu}$  is called the hadronic tensor. Eq. 1.5 is valid if we neglect double boson exchange processes; that is, processes where we have two internal virtual bosons. In Sec. 3, we will only focus on events for which we can assume no double boson exchange. This is reasonable given the uncertainties associated with nuclear effects coming from protons and neutrons, which are much larger than the loop corrections from which these double boson exchanges come from. Moreover, we will also assume point-like nuclear particles for simplicity. To illustrate how  $|\mathcal{M}|^2$  can be split into these tensors, let us finish our calculation of  $|\mathcal{M}|^2$  for the process  $e^+e^- \rightarrow \mu^+\mu^-$ .

For simplicity, let us rearrange the amplitude to look like this

$$\mathcal{M} = \frac{ie^2}{q^2} [\bar{v}^{s'}(p_2)\gamma^\mu u^s(p_1)][\bar{u}^{r'}(p_3)\gamma_\mu v^r(p_4)], \quad (1.6)$$

where we have moved the constant factors to the front and we contracted  $g_{\mu\nu}\gamma^\nu = \gamma_\mu$ . The amplitude  $\mathcal{M}$  is a complex number. To get  $|\mathcal{M}|^2$ , we need  $\mathcal{M}$  and  $\mathcal{M}^*$ , but since  $\mathcal{M}$  is just a number,  $\mathcal{M}^* = (\mathcal{M}^\dagger)^T = \mathcal{M}^\dagger$ . The Hermitian conjugate of the amplitude is

$$\mathcal{M}^\dagger = \frac{-ie^2}{q^2} [\bar{u}^s(p_1)\gamma^\nu v^{s'}(p_2)][\bar{v}^r(p_4)\gamma_\nu u^{r'}(p_3)]. \quad (1.7)$$

Since  $\mathcal{M}^\dagger = \mathcal{M}^*$ , we can put together Eq. 1.6 and Eq. 1.7 to get the squared amplitude

$$|\mathcal{M}|^2 = \frac{e^4}{q^4} [\bar{v}^{s'}(p_2)\gamma^\mu u^s(p_1)][\bar{u}^s(p_1)\gamma^\nu v^{s'}(p_2)][\bar{u}^{r'}(p_3)\gamma_\mu v^r(p_4)][\bar{v}^r(p_4)\gamma_\nu u^{r'}(p_3)], \quad (1.8)$$

where we have moved around the quantities in square brackets since they are just complex numbers. This squared amplitude  $|\mathcal{M}|^2$  is for a given set of momenta and spins. However, in real experiments, we (usually) have an unpolarized beam of incoming particles. This unpolarized beam means that any measurements are an average over the initial state spins  $s$  and  $s'$ . After the process takes place, the detectors measure the aggregated results of the interactions without differentiating between different final spin states. Therefore, any measurements are over a sum of the final state spins  $r$  and  $r'$ . With this in mind, we get

that the actual quantity we are looking for is  $\frac{1}{2} \sum_s \frac{1}{2} \sum_{s'} \sum_r \sum_{r'} |\mathcal{M}|^2 = \frac{1}{4} \sum_{s,s',r,r'} |\mathcal{M}|^2$ , which is given by

$$\frac{1}{4} \sum_{s,s',r,r'} |\mathcal{M}|^2 = \frac{e^4}{q^4} \frac{1}{4} \sum_{s,s',r,r'} [\bar{v}^{s'}(p_2) \gamma^\mu u^s(p_1)] [\bar{u}^s(p_1) \gamma^\nu v^{s'}(p_2)] \times \\ [\bar{u}^{r'}(p_3) \gamma_\mu v^r(p_4)] [\bar{v}^r(p_4) \gamma_\nu u^{r'}(p_3)].$$

We can further simplify this expression for  $\frac{1}{4} \sum |\mathcal{M}|^2$ .

Using the spin-sum relations for Dirac spinors<sup>1</sup>, the Dirac equation relations<sup>2</sup> and the trace relations<sup>3</sup>, and neglecting the masses of the electrons and muons, we obtain the following result,

$$\frac{1}{4} \sum_{s,s',r,r'} |\mathcal{M}|^2 = \frac{e^4}{q^4} \frac{1}{4} 4(p_1^\mu p_2^\nu + p_2^\mu p_1^\nu - (p_1 \cdot p_2) g^{\mu\nu}) \cdot 4(p_{3,\mu} p_{4,\nu} + p_{4,\mu} p_{3,\nu} - (p_3 \cdot p_4) g_{\mu\nu}).$$

Notice that the first term in parenthesis only depends on the momenta of the incoming electron ( $p_1$ ) and positron ( $p_2$ ), and the second term in parenthesis only depends on the momenta of the outgoing muon ( $p_3$ ) and antimuon ( $p_4$ ). We can therefore define two quantities that contain the information about the electron/positron and the muon/antimuon pairs. These quantities will be the electron leptonic tensor  $L_{e^-}^{\mu\nu}$  and the muon leptonic tensor  $L_{\mu^-,\mu\nu}$ . In this paper, we do not include the spin-average factor  $\frac{1}{4}$  into our definition of the leptonic tensors. We define them as

$$L_{e^-}^{\mu\nu} = \frac{4e^2}{q^2} (p_1^\mu p_2^\nu + p_2^\mu p_1^\nu - (p_1 \cdot p_2) g^{\mu\nu}), \quad (1.9)$$

$$L_{\mu^-,\mu\nu} = \frac{4e^2}{q^2} (p_{3,\mu} p_{4,\nu} + p_{4,\mu} p_{3,\nu} - (p_3 \cdot p_4) g_{\mu\nu}). \quad (1.10)$$

And our amplitude is given by

$$\frac{1}{4} \sum_{s,s',r,r'} |\mathcal{M}|^2 = \frac{1}{4} L_{e^-}^{\mu\nu} L_{\mu^-,\mu\nu}.$$

Although we could continue simplifying our calculation, we will stop here for now. As we have stated, the contraction of these two leptonic tensors gives us the squared amplitude summed over all of the spins (i.e.  $\sum_{s,s',r,r'} |\mathcal{M}|^2$ .) For the cases that we will be analyzing in this work, this is always the case. However, instead of having two leptonic tensors, we will have one leptonic tensor  $L_{\mu\nu}$  and one hadronic tensor  $H^{\mu\nu}$ . Conceptually, the only difference between the hadronic and the leptonic tensor is that the leptonic tensor contains the information that pertains to the leptons in the interaction. Similarly, the hadronic tensor contains the information that pertains to the hadrons in the interaction.

---

<sup>1</sup>  $\sum_{s=\pm 1/2} u_f(\vec{p}, s) \bar{u}_f(\vec{p}, s) = \not{p} + m_f$

<sup>2</sup>  $(\not{p} - m_f) u_f(\vec{p}, s) = \bar{u}_f(\vec{p}, s) (\not{p} - m_f) = 0$

<sup>3</sup>  $\text{Tr}[\gamma^\mu] = 0$ ,  $\text{Tr}[\text{odd number of } \gamma^\mu] = 0$ ,  $\text{Tr}[\gamma^\mu \gamma^\nu] = 4g^{\mu\nu}$ ,  $\text{Tr}[\gamma^\mu \gamma^\nu \gamma^\sigma \gamma^\rho] = 4(g^{\mu\nu} g^{\sigma\rho} - g^{\mu\sigma} g^{\nu\rho} + g^{\mu\rho} g^{\nu\sigma})$

For example, if we had the following process  $e^-p^+ \rightarrow e^-p^+$ , the leptonic tensor would correspond to the part in the Feynman diagram that contains the incoming and outgoing electron. On the other hand, the hadronic tensor would correspond to the part with the incoming and outgoing proton. Although conceptually similar, the hadronic and leptonic tensors differ in the complexity of their calculations. Whereas the leptonic tensor deals with point-like particles such as electrons and muons, the hadronic tensor deals with hadrons such as protons and neutrons that are made up of quarks and that usually are part of a larger nucleus. This structure means that we must take into account complex nuclear physics and nuclear form factors when dealing with particles of this type. The calculations of hadronic tensors are difficult but can be accomplished with event generators. To avoid the trouble of including calculations of hadronic tensors, our program only calculates the leptonic tensor and leaves the complex nuclear physics of hadronic tensors to the event generators. This separation into leptonic and hadronic tensors is one of the main advantages of our program. We want to separate easily calculable BSM effects from the intricate nuclear effects.

## 2 Methods

Now that we reviewed how to split a squared amplitude into its leptonic and hadronic tensor components, we can dive into the details of our program.

### 2.1 Universal FeynRules Output

Given a BSM Lagrangian, we utilize the `FeynRules` Mathematica package to calculate the vertices of a theory and store its information [14]. This output from `FeynRules` can be interfaced and exported as a `Universal FeynRules Output` (UFO) [15] file, which contains all the necessary information of the theory encoded into Python modules. More importantly, the UFO format is designed to be agnostic. That is, the program does not make any prior assumptions on the different Lorentz and color structures allowed in the theory as well as on the number of particles. Because of this lack of assumptions, the UFO file also allows for a larger compatibility with event generators, thus making it ‘universal’.

As part of this compatibility, the UFO file stores the information of the theory as instances of Python classes. In particular, all the instances of particles, parameters, Lorentz and color structures, couplings and vertices are stored in their own Python module, ready to be interfaced with computer codes. However, these objects are stored as strings that represent mathematical objects. For example, the electromagnetic vertex for  $e^+e^-$  annihilation

$$ie\gamma^\mu \tag{2.1}$$

would be stored as:

---

```
V_77 = Vertex(name = 'V_77',
              particles = [ P.e__plus__, P.e__minus__, P.a ],
              color = [ '1' ],
              lorentz = [ L.FFV1 ],
              couplings = {(0,0):C.GC_3})
```

---

with Lorentz structure

---

```
FFV1 = Lorentz(name = 'FFV1',
               spins = [ 2, 2, 3 ],
               structure = 'Gamma(3,2,1)')
```

---

and coupling

---

```
GC_3 = Coupling(name = 'GC_3',
                value = '-(ee*complex(0,1))',
                order = {'QED':1})
```

---

As we can see in the attributes `color` for the vertex class, `structure` for the Lorentz class and `value` for the coupling class, the instances are strings symbolizing mathematical expressions. In particular, we have

$$'1' = \mathbb{I}, \quad \text{'Gamma(3,2,1)'} = (\gamma^{\mu_3})_{i_2, i_1}, \quad \text{'-(ee*complex(0,1))'} = -ie.$$

To be able to use these UFO Python modules, we rely on the Sherpa event generator, since our program is based on the Comix algorithm of Sherpa. The way Sherpa incorporates UFO files into its code is with the `Sherpa-generate-model` command.

## 2.2 Berends-Giele Recursive Relations

For the calculation of the amplitudes, we utilize the Berends-Giele recursive relations [11]. Initially proposed to deal with color-ordered multi-gluon amplitude calculations, the Berends-Giele recursive relations form the basis of an algorithm that calculates scattering amplitudes by utilizing recursive currents built from the external particles. This recursive nature bolsters the efficiency and speed of the process, as it allows us to reuse currents that appear in more than one diagram. In fact, whereas a general, direct approach to calculate  $n$ -particle scattering amplitudes scales computationally as  $\mathcal{O}(n!)$ , the Berends-Giele recursive relation algorithm only scales as  $\mathcal{O}(a^n)$ , where  $a$  is the highest point vertex. Since its inception, the Berends-Giele algorithm has been extended to deal with general 3-point vertices (i.e. not just gluons), as employed in the matrix element generator Comix [20]. Furthermore, Sherpa [23] generalized these tree-level calculations with Berends-Giele to  $n$ -point vertices. We rely and build on the code developed by Ref. [23] to calculate the leptonic tensors.

The fundamental objects in the Berends-Giele recursive relations are the  $n$ -particle currents  $J_i^\mu(\pi)$ , where  $\pi$  is the set of  $n$  particles to which this current corresponds to, and  $i$  is an index labeling the current. The superscript  $\mu$  is a multi-index that represents Lorentz, spin and color indices, depending on the type of object. When a particle  $i$  is an external particle, its current  $J_i^\mu$  is given by the particle's external wavefunctions (e.g. spinors, polarization vectors, etc.) For 3-point vertices, two currents  $J_j^\nu(\pi_1)$  and  $J_k^\rho(\pi_2)$  produce a new current  $J_i^\mu(\pi)$ , where  $\pi = \pi_1 \oplus \pi_2$ . In general, a Berends-Giele 3-point current can be expressed as follows

$$J_i^\mu(\pi) = \sum_{V_i^{j,k}} \sum_{\{\pi_1, \pi_2\} \in P_2(\pi)} S(\pi_1, \pi_2) P_i(\pi) V_i^{j,k}(\pi_1, \pi_2) J_j^\nu(\pi_1) J_k^\rho(\pi_2), \quad (2.2)$$

where  $\pi_1, \pi_2$  are set partitions of  $\pi$ ,  $P_i(\pi)$  is the propagator corresponding to particle type  $i$ , and  $V_i^{j,k}$  is the 3-point vertex connecting these three currents for given partitions  $\pi_1, \pi_2$ . The sums are over all (unordered) set partitions of  $\pi$  into  $\pi_1, \pi_2$  and for all the existing 3-point vertices of the two base currents  $J_j^\nu(\pi_1)$  and  $J_k^\rho(\pi_2)$  [20]. By convention, we assume that all particles are outgoing. In that case, if a particle is incoming, we make it outgoing by flipping the direction of its momentum and changing it to its antiparticle. For example, an incoming electron  $e^-$  with momentum  $p$  would become an outgoing positron  $e^+$  with momentum  $-p$ . This convention is also adopted in the UFO vertices files.

The prefactor  $S(\pi_1, \pi_2)$  is a symmetry factor for the corresponding set partition of  $\pi$  into  $\pi_1 \oplus \pi_2$ . This symmetry factor is to account for the antisymmetry of possibly indistinguishable fermionic particles. Its value is given by:

$$S(\pi_1, \pi_2) = (-1)^{S_f(\pi_1, \pi_2)} \quad (2.3)$$

where  $S_f(\pi_1, \pi_2)$  is a function that counts the number of (fermion) permutations necessary to achieve a predefined order. By fermion permutations, we mean that, if one of the particles in  $\pi_1$  or  $\pi_2$  was not a fermion, we would not include it in our calculation of  $S_f$ .

In general, we will have that the  $n$ -particle scattering amplitude  $\mathcal{M}$  for a set of particles  $\pi$  is given by

$$\mathcal{M}(\pi) = J_i^\alpha(n) \frac{g_{\alpha\beta}}{P_{i-1}(\pi - n)} J_{i-1}^\beta(\pi - n), \quad (2.4)$$

where  $J_i^\alpha(n)$  is the current of the  $n$ th particle,  $J_{i-1}(\pi - n)$  is the current of the set  $\pi$  of all particles minus particle  $n$ , and  $P_{i-1}(\pi - n)$  is the propagator term corresponding to  $J_{i-1}(\pi - n)$ .

Similarly, the calculation of the leptonic tensor from the Berends-Giele currents is given by

$$L^{\mu\nu} = \sum_{\text{helicity states}} (J_i^\mu) \otimes (J_i^\nu)^\dagger, \quad (2.5)$$

where  $J_i$  is the current that corresponds to the leptonic tensor,  $\dagger$  is the Hermitian conjugate operator and  $\otimes$  is the outer tensor product operator.

A schematic of the recursive process for the amplitude calculation is given in Fig. 2. In this figure, we see a recursive break down of currents into subcurrents that make up the Feynman diagram. It is imperative to point out, however, that the algorithm starts with the external currents and builds up the Feynman diagrams from there instead of starting with the Feynman diagrams and breaking them down into external currents as the figure might lead one to believe.

### 2.3 Multichannel Monte Carlo Phase Space Integration

One of the main advantages of our program is that it will let us focus only on the new physics within the leptonic tensor, leaving the calculation of the complicated hadronic tensor to the event generators. However, to prove that our program is calculating the leptonic tensors correctly, we must compare and validate our results with already-calculated examples in the literature. These examples, however, tend to come as cross sections or differential

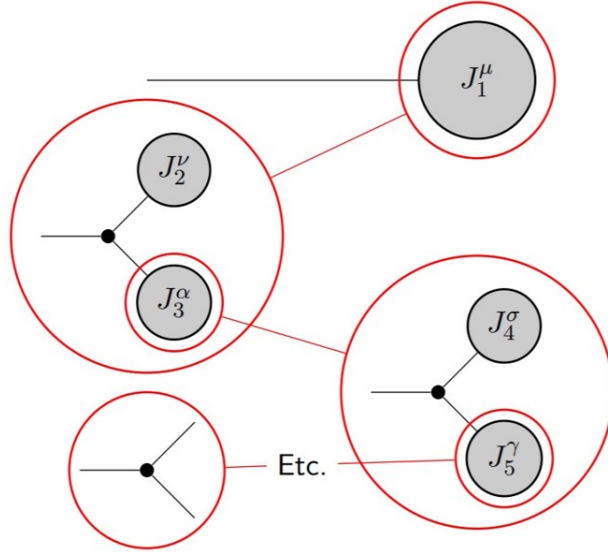


**Figure 2.** Schematic of the recursive nature of the Berends-Giele recursive relations. Each current  $J_i^\mu$  is built from other subcurrents  $J_2^\nu, J_3^\alpha$ , etc., with base case being the external wavefunctions.

cross sections for which we require the squared matrix element  $|\mathcal{M}|^2$ . As was shown in Sec. 1.3, to obtain  $|\mathcal{M}|^2$  from the leptonic tensor, we also need the hadronic tensor, if only momentarily. For the implementation of the hadronic tensor, we rely on Ref. [29], where the development of a hadronic tensor taking into account the nuclear physics effects is discussed in detail. With that issue resolved, our next task is to obtain the cross section. From Sec. 1.1, we know that the cross section  $\sigma$  is proportional to the integral over phase space of the squared matrix element. That is,

$$\sigma(A_1 A_2 \rightarrow B_1 B_2 \cdots B_n) = \frac{S}{2\sqrt{\lambda(E_{CM}^2, m_{A_1}^2, m_{A_2}^2)}} \int d\Pi_n |\mathcal{M}|^2. \quad (1.1)$$

However, as  $n$  grows larger, the integral over phase space becomes extremely difficult to solve. A way around this issue is to numerically solve this integral. For this numerical approach, we rely on Monte Carlo integration techniques. Specifically, we focus on the multichannel Monte Carlo integration [25] of our squared matrix element in phase space.

Monte Carlo techniques rely on random sampling to estimate results. For our integrals, we randomly sample points over our integration region (i.e. phase space) and obtain an estimate of the integral by calculating the expectation value of a weight function that is related to  $|\mathcal{M}|^2$ .

Suppose we have a function  $f(x)$  that we want to integrate over some domain  $\mathcal{X}$ ,

$$I = \int_{\mathcal{X}} f(x) dx. \quad (2.6)$$

In general, we would have a random variable  $X(x)$  that maps  $x$  to random numbers according to a uniform distribution in  $\mathcal{X}$ ; that is  $X \sim \text{Unif}(\mathcal{X})$ . We take  $N$  samples  $(x_1, x_2, \cdots, x_N)$  of the random variable  $X$  on  $\mathcal{X}$  and call the function  $f$  on these samples

(i.e.  $f(x_i)$ ). The estimate of  $I$  is proportional to the expectation value of  $f(x)$  on these samples; that is

$$I \approx c \langle f(x) \rangle = c \frac{1}{N} \sum_{i=1}^N f(x_i), \quad (2.7)$$

where  $c$  is a constant of proportionality.

In the multichannel approach, instead of having one random variable, we have several. The structure of the matrix element tends to have some defined peaks throughout regions of phase space that depend on different phase space variables. Having different random variables allows us to have mappings that focus on a specific peak or feature of the matrix element function. Let us label these random variables by  $X_i(x)$ . Each of these random variables represents a channel, hence the multichannel nomenclature, and have a non-uniform probability distribution function  $g_i(x)$ . The selection of which distribution will be used is randomly selected event-by-event and depends on probabilities given by a-priori weights  $\alpha_i$ . That is, the probability of selecting random variable  $X_i$  for the sampling is  $\alpha_i$ , where  $\sum_i \alpha_i = 1$ . The total probability density for a given sample is then given by

$$g(x) = \sum_{i=1}^N \alpha_i \cdot g_i(x). \quad (2.8)$$

The Monte Carlo integration points are then distributed according to  $g(x)$ . Let us now define a weight function for each Monte Carlo point given by

$$w(x) = \frac{f(x)}{g(x)}. \quad (2.9)$$

Notice then that the expectation value of this weight function gives us the estimate for our integral  $I$ ,

$$\langle w(x) \rangle = \int_{\mathcal{X}} w(x) g(x) dx = \int_{\mathcal{X}} \frac{f(x)}{g(x)} g(x) dx = \int_{\mathcal{X}} f(x) dx. \quad (2.10)$$

Once we have the set of  $N$  samples  $\{x_i\}$ , we can calculate  $\langle w(x) \rangle$  based on these values.

One of the key features of the multichannel approach is its ability to reduce the error estimate of the integral. For the multichannel, the expected error is given by

$$\delta I = \frac{1}{\sqrt{N}} \sqrt{\int_{\mathcal{X}} \frac{f(x)^2}{g(x)} dx - \left( \int_{\mathcal{X}} f(x) dx \right)^2}. \quad (2.11)$$

Notice that  $\delta I$  depends on  $g(x)$ , which in turn depends on  $\alpha_i$ . Thus, by optimizing the a-priori weights  $\alpha_i$ , one can reduce the expected error without having to increase the number of samples  $N$ .

Before finishing this section, it is worth making more of a connection of this method to the case at hand. For matrix elements, one of the ways to focus on the distinct features and peaks is through the function's dependence on Mandelstam variables. A matrix element can depend on more than one Mandelstam variable and the shape of the function can be heavily influenced by some variables more than others at different intervals of the

integration domain. Hence, one could have different random variables and distributions that accurately map the structure produced by an  $s$ -,  $t$ - or  $u$ -channel diagram, as well as their interference. Depending on the process we are dealing with, we could optimize the  $\alpha_i$ 's to give more weight to one variable over the others.

## 2.4 VEGAS Algorithm

As mentioned in the previous section, the multichannel Monte Carlo phase space integrator is our approach at numerically estimating the cross section, given as the integral of the squared matrix element  $|\mathcal{M}|^2$  over phase space. One of the features of the multichannel integrator is the use of several different probability distributions  $g_i(x)$  that span our integration region to account for the different peaks in the structure of  $|\mathcal{M}|^2$ . Based on our knowledge of  $|\mathcal{M}|^2$ , we can specify the  $g_i(x)$ 's to cover these peaks. However, it is generally harder to account for the interference terms between Mandelstam variables and it is also possible that our integrand function has experimental cuts that we are unable to take into account directly into our definitions of the  $g_i(x)$ 's. To solve this, we rely on the VEGAS algorithm [28].

VEGAS works by mapping the original integration variables  $\vec{x}$  over the range  $[a, b]$  to another set of integration variables  $\vec{y}$  over the range  $[0, 1]$ . This mapping is done by dividing each of the axes of  $\vec{x}$  into  $N_g$  intervals with varying interval widths  $\delta\vec{x}_i$ . These intervals of varying width in  $\vec{x}$  map to intervals of constant width in  $\vec{y}$ . The optimal grid of  $\vec{y}$  occurs when the average value of  $J^2(\vec{y}(\vec{x})) \cdot f^2(\vec{x})$  is the same in every interval width  $\delta\vec{x}_i$ , where  $J(\vec{y}(\vec{x}))$  is the Jacobian of the transformation from  $\vec{x}$  to  $\vec{y}$ . The Jacobian at this optimal grid flattens out the peaks in  $\vec{y}$  and spreads them out. The result of this flattening is that a uniform distribution of points in  $\vec{y}$  corresponds to a distribution of points in  $\vec{x}$  that has a higher density around areas of peaks. Once optimized, VEGAS estimates the value of the integral using the corresponding transformation with the optimized Jacobian.

Multichannel and VEGAS interact by assigning each channel  $g_i(x)$  to a VEGAS integrator. This assignment takes advantage of VEGAS' ability to incorporate experimental cuts into its estimate of the integral and its strength in dealing with single- to few-peaks structures. In this way, we capitalize on VEGAS' and multichannel's particular strengths to produce a better estimate of the integral. With multichannel, we have the ability to use our prior knowledge of  $|\mathcal{M}|^2$  and its relation to Mandelstam variables to specify appropriate channels  $g_i(x)$ , and we use VEGAS to deal with each  $g_i(x)$  and other unknown features of  $|\mathcal{M}|^2$ .

## 2.5 BSM Models to UFO Files

Before ending this section, let us briefly discuss about how different BSM models are turned into UFO files.

For this conversion process, we rely on the `FeynRules` Mathematica package [9] to produce UFO files. We start by writing a `FeynRules` model format (`.fr`) text file that contains the relevant information about the model. For simplicity, let us focus on one of the models we converted, the Dark Neutrino Portal to Explain MiniBooNE Excess [12]. For this model, we added the relevant new physics information to our `.fr` file. For example, this model adds a dark  $Z$  boson,  $Z_{\mathcal{D}}$ , and a dark neutrino,  $\nu_{\mathcal{D}}$ , that interact with the SM

particles via kinetic and mass mixing for  $Z_{\mathcal{D}}$  and neutrino mixing for  $\nu_{\mathcal{D}}$ . Along with these interactions, we need a dark coupling and some mixing parameters that are implemented in the model file. For the dark coupling  $\alpha_{\mathcal{D}}$ , for example, we have

---

```
M$Parameters = {
  aD == {
    ParameterType -> External,
    Value         -> 0.25,
    InteractionOrder -> {NP, 1},
    Description    -> "Dark coupling constant"
  },
  ...
}
```

---

As we can see, we must specify the type of parameter (external, internal), its value, its interaction order (NP stands for New Physics) and a short description.

We must also add the particles of this model,  $Z_{\mathcal{D}}$  and  $\nu_{\mathcal{D}}$ , to the text file. For  $Z_{\mathcal{D}}$ , we have

---

```
M$ClassesDescription = {
  V[100] == {
    ClassName      -> ZD,
    SelfConjugate  -> True,
    Mass           -> {MZD, 0.03},
    Width          -> {WZD, 1.0},
    ParticleName   -> "Z_D",
    PropagatorLabel -> "Z_D",
    PropagatorArrow -> None,
    FullName       -> "Dark Z"
  },
  ...
}
```

---

where we must specify whether the particle is its own antiparticle (`SelfConjugate ->True`), its mass and width, as well as information about the particle's formatting in Feynman diagrams.

With the model text file implemented, we proceed to calculate the Feynman vertices with Mathematica. In Mathematica, we implement the Lagrangian of our theory, which in this case is given by

$$\mathcal{L}_{\mathcal{D}} \supset \frac{m_{Z_{\mathcal{D}}}^2}{2} Z_{\mathcal{D}\mu} Z_{\mathcal{D}}^{\mu} + g_{\mathcal{D}} Z_{\mathcal{D}}^{\mu} \bar{\nu}_{\mathcal{D}} \gamma_{\mu} \nu_{\mathcal{D}} + e \epsilon Z_{\mathcal{D}}^{\mu} J_{\mu}^{\text{em}}, \quad (2.12)$$

where  $m_{Z_{\mathcal{D}}}$  is the mass of the  $Z_{\mathcal{D}}$  and  $g_{\mathcal{D}} = \sqrt{4\pi\alpha_{\mathcal{D}}}$  is the dark coupling, and  $\epsilon$  parametrizes the kinetic mixing of  $Z_{\mathcal{D}}$  with the electromagnetic current.

Once we implement  $\mathcal{L}_{\mathcal{D}}$  and combine it with the SM Lagrangian, `FeynRules` proceeds to calculate the Feynman vertices of our theory. Finally, once the calculation is done, we export the information of the theory, including particles, parameters and vertices, as a UFO file, by issuing the command `WriteUFO[L]`, where  $L$  is the Lagrangian.

### 3 Results and Discussion

To test our program, we will focus on two Standard Model processes outlined below:

1.  $e^- p^+ \rightarrow e^- p^+$  with a virtual  $\gamma$  boson.
2.  $\nu_e p^+ \rightarrow \nu_e p^+$  with a virtual  $Z$  boson.

Before continuing, it is worth pointing out that the results shown in this section are from a previous version of our program. This is because, for the most up-to-date version of our program, we still have not been able to get some results. However, examining the performance of our previous version is still worthwhile to understand how our program works and the progress that we have made. The main differences between the previous version and the current one is that, in the previous version, 1) the nucleus and hadrons are treated as point-like particles with no nuclear effects, and 2) the integration method is based on the `Rambo` algorithm [24]. Regarding 1), this means that our hadronic tensor in the results shown here differs from the hadronic tensor by Dr. Rocco [29] outlined in Sec. 2.3. In terms of 2), the difference lies in the phase space integration approach, where the Multichannel approach has a better performance than `Rambo`.

For each of these processes, we will calculate the analytic and numerical squared amplitudes  $\mathcal{M}$  and plot their initial-spin averaged, final-spin summed squared amplitude versus  $\cos\theta$ , the cosine of the polar angle of the outgoing lepton. These amplitude plots will be at six different center-of-mass energies  $E_{CM}$  of 20 GeV, 60 GeV, 100 GeV, 140 GeV, 180 GeV and 200 GeV. For the numerical result, we will use our program to calculate the leptonic tensor  $L_{\mu\nu}$  and we will contract it with a general hard-coded hadronic tensor  $H^{\mu\nu}$ . The general form of  $H^{\mu\nu}$  used for these processes is given below:

$$H^{\mu\nu} = 2 \left( (g_L^2 + g_R^2) \cdot (p_1^\mu p_2^\nu + p_2^\mu p_1^\nu - (p_1 \cdot p_2) g^{\mu\nu}) + (g_L^2 - g_R^2) \cdot i \cdot \varepsilon^{\mu\nu\alpha\beta} p_{1,\alpha} p_{2,\beta} \right)$$

where  $g_L$  and  $g_R$  are the left- and right-handed couplings of the interacting particle,  $p_1, p_2$  are the momenta and  $\varepsilon^{\mu\nu\alpha\beta}$  is the totally antisymmetric Levi-Civita tensor. For this work, we take the convention that  $\varepsilon^{0123} = +1$ . Because of the way that our program was structured, we could only account for one type of virtual boson at a time both for the leptonic and for the hadronic tensors. The consequence of this is that for a process like  $e^- p^+ \rightarrow e^- p^+$ , we will only consider the photon  $\gamma$  and will ignore the  $Z$  boson. We will start our discussion of the results with process 1.

#### 3.1 $e^- p^+ \rightarrow e^- p^+$

Let us start with the scattering of an electron  $e^-$  with a proton  $p^+$ . To calculate the squared amplitude  $|\mathcal{M}|^2$  for this process, we will rely on some assumptions that will simplify our calculations. In real experiments, the proton is usually bound to a nucleus that contains other protons and neutrons. Moreover, unlike the electron, the proton is not a point-like particle but rather is composed of two up quarks and one down quark. To account for the internal structure of the proton and its bound state within the nucleus, we would need to include nuclear form factors and complex nuclear physics in our calculations. Although we

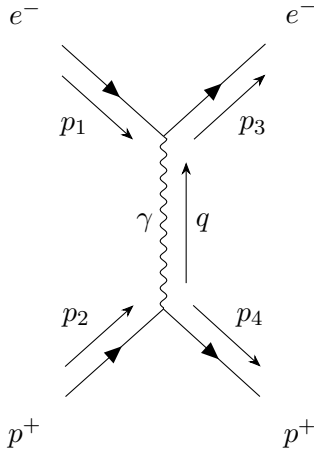


**Figure 3.** Tree-level Feynman diagram of  $e^- p^+ \rightarrow e^- p^+$  for particles with 4-momenta  $p_1, p_2, p_3, p_4$ .

do take these factors into account in our up-to-date version, in this section we will assume that the proton is a point-like, massless particle.

With these assumptions, we can compute the analytic amplitude. First, let us consider the type of Feynman diagram that we would be dealing with. The proton is a spin-1/2 fermion with positive charge +1. Based on these properties, we can assume that there exists a QED vertex coupling a photon  $\gamma$  with a proton/antiproton pair with value  $+ie\gamma^\mu$ . Since the electron and the proton are different species of particles, we can also assume that there is no QED vertex coupling a photon with these two particles, just like there is no QED vertex coupling an electron with a particle of a different species, such as the muon. Under these assumptions, our only allowed Feynman diagram would be given by: Following a similar line of reasoning, we could argue that there exists a Feynman diagram like the one in Fig. 3 but with a  $Z$  boson replacing the photon  $\gamma$ . However, as mentioned at the beginning of this chapter, we will only focus on one type of virtual boson at a time. For this process, we will only focus on the photon case.

From the Feynman diagram in Fig. 3 and from the Feynman rules, we can write down an expression for  $\mathcal{M}$  as

$$\mathcal{M} = \frac{-ie^2}{q^2} \bar{u}^r(p_3) \gamma^\mu u^s(p_1) \bar{u}^{r'}(p_4) \gamma_\mu u^{s'}(p_2).$$

From this expression for the amplitude  $\mathcal{M}$ , we can obtain a formula for  $|\mathcal{M}|^2$ . As in Sec. 1.3, we obtain the initial-state averaged, final-state summed squared amplitude by using the spin-sum relations for Dirac spinors, the Dirac equation relations and the trace relations. The resulting expression is given by

$$\frac{1}{4} \sum_{s,s',r,r'} |\mathcal{M}|^2 = \frac{8e^4}{q^4} ((p_1 \cdot p_2)(p_3 \cdot p_4) + (p_1 \cdot p_4)(p_2 \cdot p_3)). \quad (3.1)$$

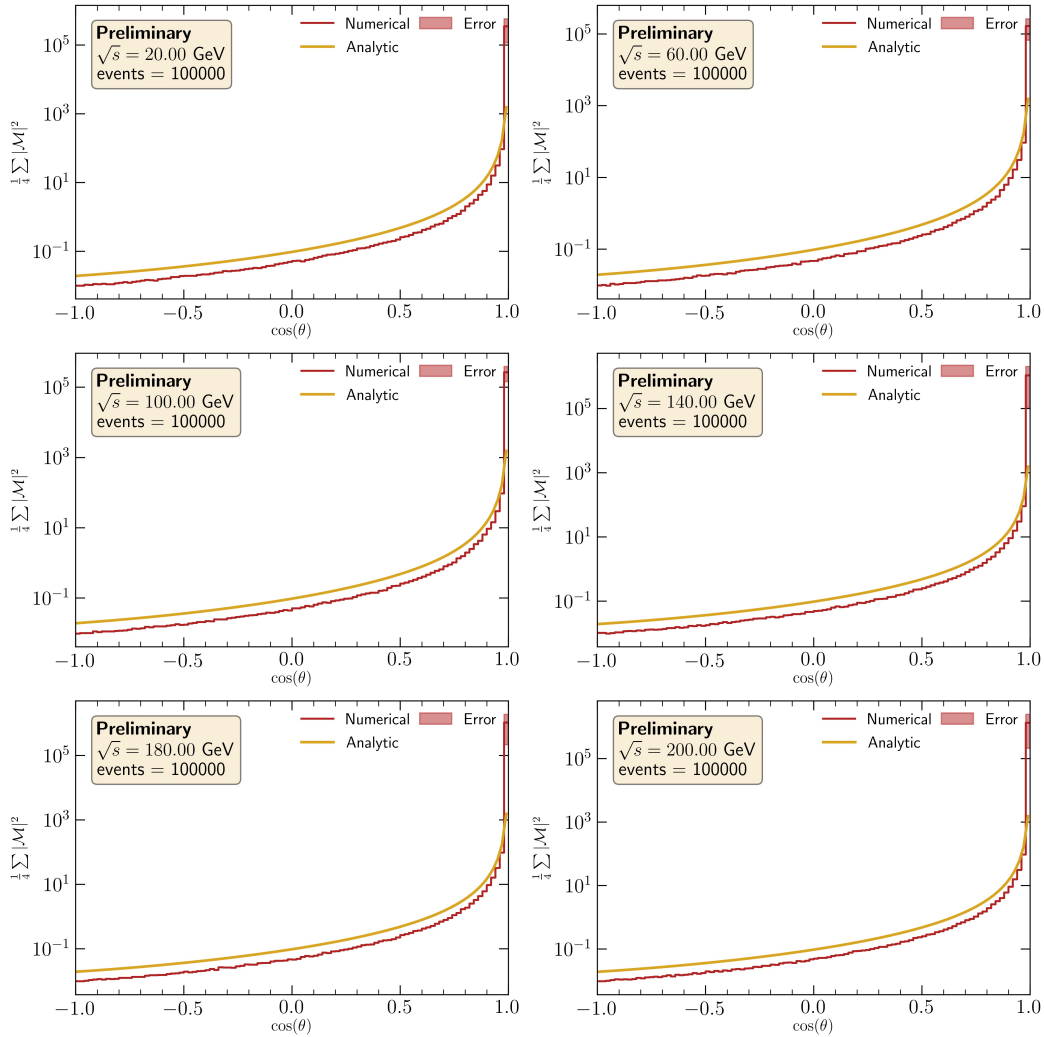


**Figure 4.** Numerical and analytic  $\frac{1}{4}|\mathcal{M}|^2$  vs.  $\cos(\theta)$  for the process  $e^-p^+ \rightarrow e^-p^+$ . For each histogram, we used  $10^5$  number of events per value of  $E_{CM}$  divided into 100 bins. From left to right, top to bottom, the center-of-mass energies are 20, 60, 100, 140, 180 and 200 GeV. The analytic values were computed from Eq. 3.2.

By focusing on the center-of-mass frame, we can further simplify Eq. 3.1 to obtain

$$\frac{1}{4} \sum_{s,s',r,r'} |\mathcal{M}|^2 = 2e^4 \left( \frac{4 + (1 + \cos \theta)^2}{(1 - \cos \theta)^2} \right). \quad (3.2)$$

This equation is our final result for the analytic amplitude of the process  $e^-p^+ \rightarrow e^-p^+$ . The result depends on the polar angle  $\theta$  and is independent of  $E_{CM}$ . As we can see from the denominator of Eq. 3.2, our amplitude blows up as  $\cos \theta \rightarrow 1$ . We will deal with this pole in the numerical calculation of our cross section. We can now compare the analytic value from Eq. 3.2 to the results from our program.

For our program, we calculated the leptonic tensor  $L^{\mu\nu}$  associated with the process  $e^-p^+ \rightarrow e^-p^+$  and contracted it with its corresponding hadronic tensor as given at the

beginning of this chapter. We performed this calculation for a range of center of mass energies from 20 GeV to 200 GeV with 190 evenly spaced samples and for a total of  $10^5$  events per value of  $E_{CM}$ . The results of these calculations were plotted in 6 histograms with 100 bins each, along with a plot of the analytic calculations. These histograms can be found in Fig. 4. As we can see, the analytic and computational values agree for the most part for all six of the histograms. Although there is a slight deviation of our numerical values from the analytic ones, we believe these to be coming from the precision of our momentum generator or from the machine. Regardless, this deviation should go away as we improve the accuracy of our program. The analytic and numerical curves are also independent of the center-of-mass energies, as expected from Eq. 3.2. In the plots, we have shown the complete range of  $\cos\theta$  values. However, for the calculation of the cross section, we will apply a cut on the values of  $\cos\theta$ . To prevent the large numbers to interfere with our cross section calculation, we added a cut  $\cos\theta < 0.95$ . Physically, the events where  $\cos\theta = 1$  (and hence  $\theta = 0$ ) are those where the particles do not interact. We are not interested in these types of events and we can safely ignore them. Let us now calculate the total cross section.

In Sec. 1.1, we saw the general form of the cross section in Eq. 1.1. For the cases of 2 incoming and 2 outgoing massless particles, this equation can be further simplified without any knowledge of the amplitude. In the end, our cross section will be proportional to  $\int d\Omega |\mathcal{M}|^2$ . However, the 2-to-2 events we are considering are symmetric around the  $z$  axis, which translates as being independent of the azimuthal angle  $\phi$ . Since  $d\Omega = d\phi d\cos\theta$ , we can also evaluate the  $\phi$  integral from  $\int d\Omega = \int_0^{2\pi} d\phi \int_{-1}^{+1} d\cos\theta$ . Finally, we need to take into account the way our detector works. As mentioned in Sec. 1.3, we need to average over the initial state spins and sum over the final state spins. When we measure the cross section, we take this into account by integrating over the initial-state spin-averaged, final-state spin-summed amplitude. Our expression for the cross section is then given by

$$\sigma = \frac{1}{32\pi E_{CM}^2} \int_{-1}^1 d\cos\theta \frac{1}{n} \sum |\mathcal{M}|^2, \quad (3.3)$$

where  $\frac{1}{n}$  is the spin average term. For  $e^-p^+ \rightarrow e^-p^+$ ,  $\frac{1}{n}$  is equal to  $\frac{1}{4}$ . To compare the cross section with our numerical results, we must integrate along the same range of values for  $\cos\theta$ . Integrating over this new range  $[-1, 0.95)$  also prevents our integral from diverging. Plugging in the expression for  $\frac{1}{4} \sum |\mathcal{M}|^2$  from Eq. 3.2 into Eq. 3.3, we can obtain the analytic result of the cross section. The integral is evaluated using `Mathematica`. For the numerical cross section, we first applied our cut to the squared amplitudes. We then used our phase space integrator `Rambo` from Ref. [24]. `Rambo` generates the random momenta that we use in our calculation of the amplitudes and it also assigns a weight to each numerical amplitude value. These weights represent the phase space factor  $\frac{1}{16\pi} d\Omega$  and we multiply them with our numerical amplitude in the cross section calculation. To get the correct numerical cross section for a given value of  $E_{CM}$ , we must average over the range of  $\cos\theta$  and divide by a flux factor equal to  $2E_{CM}^2$ . So far, we have been working in natural units where fundamental constants such as  $\hbar$  and  $c$  are set equal to 1 and all quantities are expressed in terms of energy. However, when we measure the cross section, we do so in

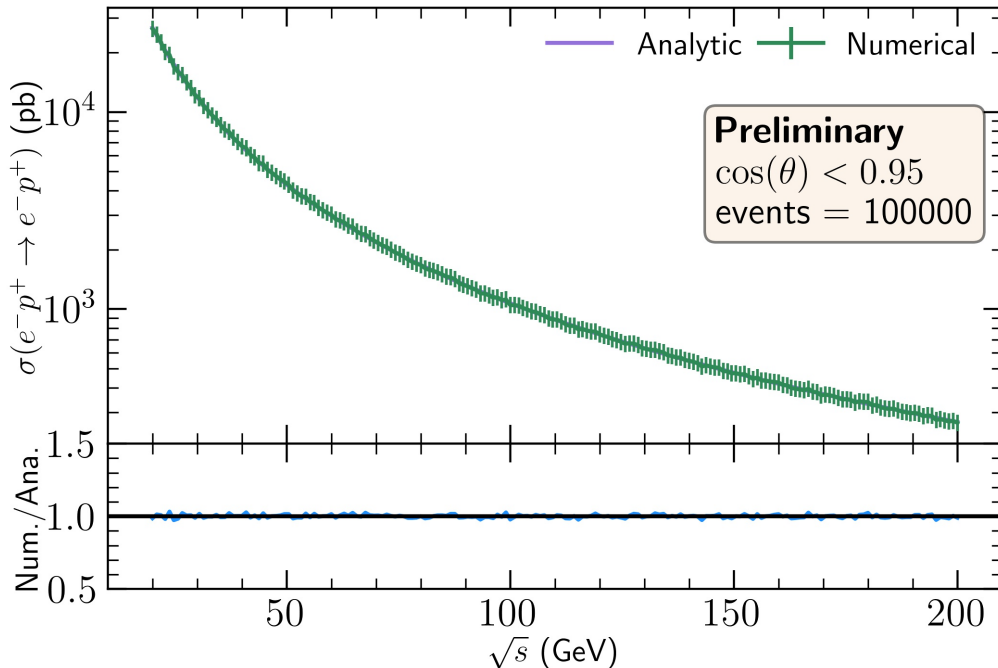


**Figure 5.** Cross section  $\sigma$  for the process  $e^-p^+ \rightarrow e^-p^+$  as a function of center-of-mass energy  $E_{CM} = \sqrt{s}$ . For each of the 190 evenly spaced values of  $E_{CM}$ , we calculated  $\frac{1}{4}|\mathcal{M}|^2$  with  $10^5$  events.

squared meters. Because the cross sections are very small quantities, we rely on the unit barn (b) where  $1 \text{ b} = 1 \times 10^{-28} \text{ m}^2$ . For our examples, we will be expressing  $\sigma$  in units of pb where the pico prefix is equivalent to  $10^{-12}$ . As can be seen from Eq. 3.3, the cross section  $\sigma$  is given in units  $\text{GeV}^{-2}$ . To recover pb from our natural units, we must multiply by the conversion factor  $(\hbar c)^2 = 1 \text{ GeV}^{-2} = 0.38937966 \times 10^9 \text{ GeV}^2 \text{ pb}$ . Thus, we get the numerical results for the cross section. For  $e^-p^+ \rightarrow e^-p^+$ , the results can be found in Fig. 5. As we can see in the figure, the analytic and numerical cross sections agree very well throughout the range of energies [20 GeV, 200 GeV]. This agreement can be seen in the subplot at the bottom of the figure. This subplot is the numerical to analytic ratio and it stays constantly near 1 with very small fluctuations. We can also see from the plot the  $E_{CM}^{-2}$  dependence of our cross section, as was expected. This concludes our analysis of the electron proton scattering.

### 3.2 $\nu_e p^+ \rightarrow \nu_e p^+$

Our second process is the electron neutrino proton scattering  $\nu_e p^+ \rightarrow \nu_e p^+$ . Like in Sec. 3.1, we will assume that the proton is a massless, point-like particle and we will start this section with the analytic calculation of the amplitude. The neutrino only interacts via the  $W^\pm$  and  $Z$  bosons. For this process, the only possibility for the neutrinos to interact is with each other via the  $Z$  boson. Similarly, the  $Z$  boson can interact with the proton/antiproton pair. Thus, the only tree-level Feynman diagram for this process would be given by: With this Feynman diagram, we can proceed to write down the amplitude.

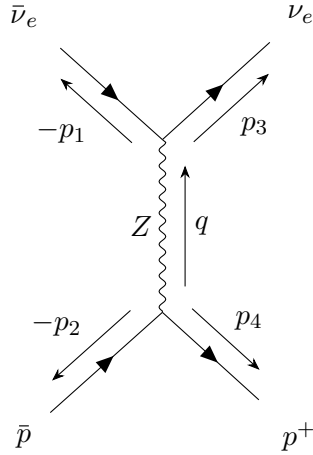


**Figure 6.** Tree-level Feynman diagram of  $\nu_e p^+ \rightarrow \nu_e p^+$  for particles with 4-momenta  $p_1, p_2, p_3, p_4$ . In this case, all particles are considered outgoing, transforming the incoming  $\nu_e$  and  $p^+$  into  $\bar{\nu}_e$  and  $\bar{p}$ , respectively, and flipping their momenta.

First, we must know the vertex factor coming from the  $Z$  boson. The coupling of the  $Z$  boson is given by  $ig_Z$  where  $g_Z = \frac{e}{\sin\theta_W \cos\theta_W}$ . However, unlike the photon, the coupling of the  $Z$  to left- and right-handed fermions is different and it is given by

$$g_L = ig_Z(I_3^f - \sin^2\theta_W Q_f),$$

$$g_R = ig_Z(-\sin^2\theta_W Q_f),$$

where  $I_3^f$  is the isospin of the fermion,  $Q_f$  is its electric charge, and  $g_Z$  is the  $Z$  boson coupling. We can calculate now the couplings specific to the neutrinos and the protons. Neutrinos have no electric charge and their isospin is  $+\frac{1}{2}$ . Given that their electric charge is 0, the right-handed coupling of neutrinos to the  $Z$  boson is 0, as expected since we only allow left-handed neutrinos. The left coupling for neutrinos is given by  $g_{L,\nu} = \frac{ie}{2\sin\theta_W \cos\theta_W}$ . Protons, on the other hand, do have an electric charge of  $+1$  and their isospin is also  $+\frac{1}{2}$ . So, their left coupling to the  $Z$  is given by  $g_{L,p} = \frac{ie}{\sin\theta_W \cos\theta_W} \left(\frac{1}{2} - \sin^2\theta_W\right) = ie \left(\frac{\cos\theta_W}{2\sin\theta_W} - \frac{\sin\theta_W}{2\cos\theta_W}\right)$ . The right coupling is given by  $g_{R,p} = -ie \frac{\sin\theta_W}{\cos\theta_W}$ . To differentiate between left- and right-handed couplings, we must include a projector with each term. Putting these results together, we arrive at the vertices for our diagram

$$\begin{array}{c} \bar{\nu}_e \\ \swarrow \\ \nu_e \end{array} \begin{array}{c} \nu_e \\ \swarrow \\ \bar{\nu}_e \end{array} = \frac{ie}{2\sin\theta_W \cos\theta_W} \gamma^\mu P_L, \quad (3.4)$$

$$\begin{array}{c} \bar{p} \\ \swarrow \\ p^+ \end{array} \begin{array}{c} p^+ \\ \swarrow \\ \bar{p} \end{array} = \left( ie \left( \frac{\cos\theta_W}{2\sin\theta_W} - \frac{\sin\theta_W}{2\cos\theta_W} \right) \gamma^\mu P_L \right) + \left( -ie \frac{\sin\theta_W}{\cos\theta_W} \gamma^\mu P_R \right). \quad (3.5)$$

Lastly, the  $Z$  boson will have a propagator that takes into account its mass and finite lifetime. The expression for the  $Z$  boson propagator is

$$\mu \begin{array}{c} Z \\ \text{~~~~~} \\ \xrightarrow{q} \end{array} \nu = \frac{-ig_{\mu\nu}}{(q^2 - M_Z^2) - iM_Z\Gamma_Z}. \quad (3.6)$$

We can now put our results from Eq. 3.4, Eq. 3.5, Eq. 3.6 together with the Feynman rules from Sec. 1.2 to write down an expression for our amplitude

$$\begin{aligned} \mathcal{M} &= \bar{u}^r(p_3)g_{L,\nu}\gamma^\mu P_L u^s(p_1) \times \\ &\quad \frac{-ig_{\mu\nu}}{(q^2 - M_Z^2) - iM_Z\Gamma_Z} \times \\ &\quad \bar{u}^{r'}(p_4)(g_{L,p}\gamma^\nu P_L + g_{R,p}\gamma^\nu P_R) u^{s'}(p_2) \\ &= \frac{-i}{(q^2 - M_Z^2) - iM_Z\Gamma_Z} \bar{u}^r(p_3)g_{L,\nu}\gamma^\mu P_L u^s(p_1) \bar{u}^{r'}(p_4)(g_{L,p}\gamma_\mu P_L + g_{R,p}\gamma_\mu P_R) u^{s'}(p_2), \end{aligned}$$

where I have directly written down the expression with the incoming spinors. Neutrinos only contribute a  $\frac{1}{2}$  term to the spin average. However, the proton is not limited like the neutrino and contributes a factor of  $\frac{1}{2}$  to the spin average term. The spin averaged and summed amplitude is therefore

$$\frac{1}{2} \sum_{s,s',r,r'} |\mathcal{M}|^2 = \frac{8g_{L,\nu}^2}{(q^2 - M_Z^2)^2 + M_Z^2\Gamma_Z^2} (g_{L,p}^2(p_1 \cdot p_2)(p_3 \cdot p_4) + g_{R,p}^2(p_1 \cdot p_4)(p_2 \cdot p_3)). \quad (3.7)$$

Focusing again on the center-of-mass frame, we arrive at the following result

$$\begin{aligned} \frac{1}{2} \sum_{s,s',r,r'} |\mathcal{M}|^2 &= \frac{e^4}{8 \cos^4 \theta_W \sin^4 \theta_W} \frac{1}{\left(\frac{E_{CM}^2}{2}(1 - \cos \theta) + M_Z^2\right)^2 + (M_Z^2\Gamma_Z^2)} \times \\ &\quad E_{CM}^4(1 - 4 \sin^2 \theta_W \cos^2 \theta_W + \sin^4 \theta_W(1 + \cos \theta)^2). \end{aligned} \quad (3.8)$$

This equation is our final result for the analytic amplitude of the process  $\nu_e p^+ \rightarrow \nu_e p^+$ . The result depends on both the polar angle  $\theta$  and the center-of-mass energy  $E_{CM}$ , as well as the mass and decay width of the  $Z$  boson. We can now compare the analytic value from Eq. 3.8 to the results of our program.

Like in the previous sections, we calculate the leptonic tensor  $L^{\mu\nu}$  associated with our process  $\nu_e p^+ \rightarrow \nu_e p^+$  and contract it with its corresponding hadronic tensor, dividing by 2 to account for the spin average term. The range for our center-of-mass energies goes from 20 GeV to 200 GeV with 190 evenly spaced samples and for a total of  $10^5$  events per value of  $E_{CM}$ . We plotted our results in 6 histograms with 100 bins each along with plots of the analytic calculations. The six values of  $E_{CM}$  are given at the beginning of this chapter and can also be found within the each plot. The histograms can be found in Fig. 7. As we can see, our analytic and numerical results do not match at any point of the range of  $\cos \theta$ . However, the numerical plot follows the same behavior as the analytic and it is off by about a factor of 2. As we found out, the error in the histogram was only due to a missing

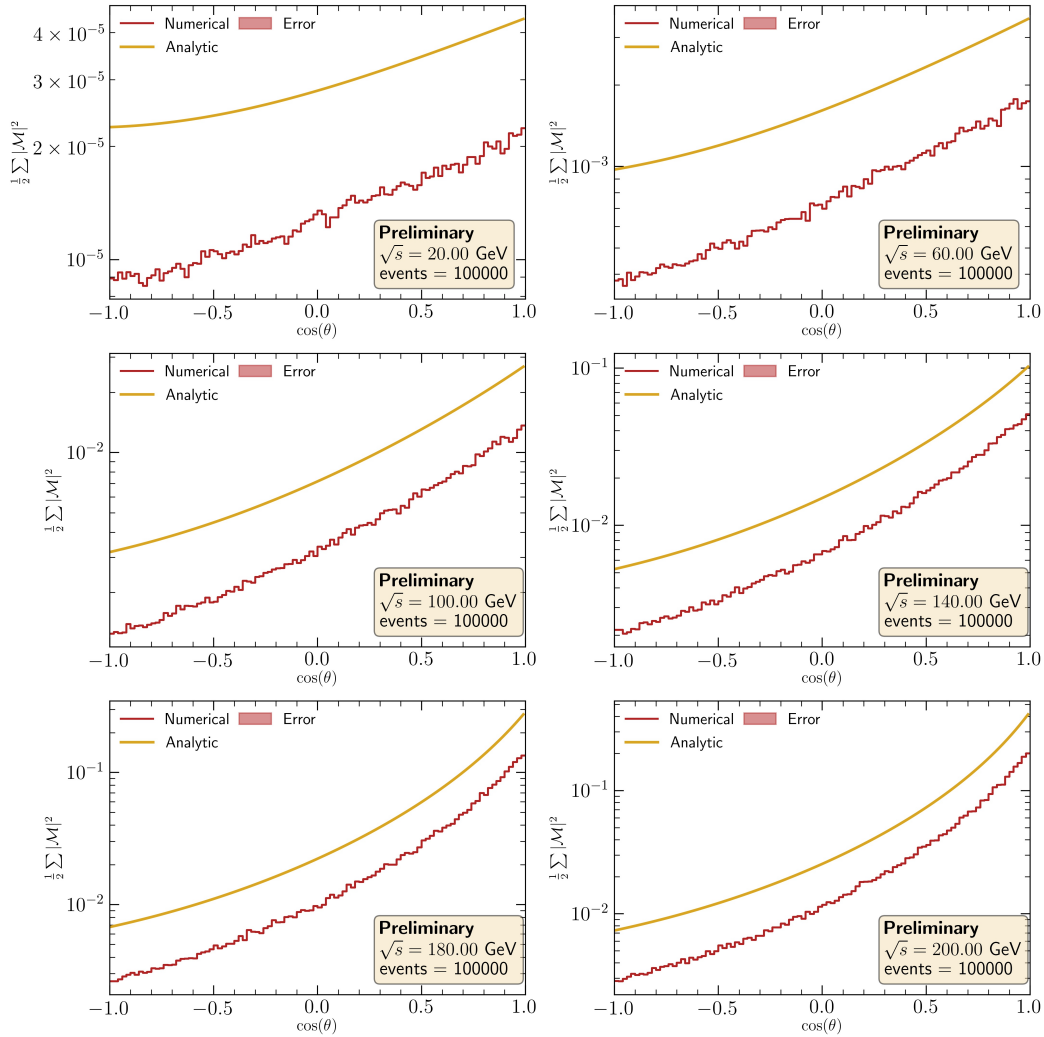


**Figure 7.** Numerical and analytic  $\frac{1}{2} \sum |\mathcal{M}|^2$  vs.  $\cos(\theta)$  for the process  $\nu_e p^+ \rightarrow \nu_e p^+$ . For each histogram, we used  $10^5$  number of events per value of  $E_{CM}$  divided into 100 bins. From left to right, top to bottom, the center-of-mass energies are 20, 60, 100, 140, 180 and 200 GeV. The analytic values were computed from Eq. 3.8.

normalization factor in the way we plotted our histograms. We shift our focus now to the cross section.

As usual, our cross section is given by Eq. 3.3 where our spin average term is  $\frac{1}{2}$  as explained earlier. Our amplitude does not blow up as  $\cos \theta \rightarrow 1$ , so we do not need a cut on the cosine. To obtain the analytic cross section, we follow our usual procedure of integrating over the range  $[-1, 1]$  for  $\cos \theta$  using *Mathematica* and multiplying by the conversion factor from  $\text{GeV}^{-2}$  to pb. For the numerical cross section, we follow the same method outlined in Sec. 3.1. We average over our range of  $\cos \theta$ , divide by our flux factor  $2E_{CM}^2$  and multiply by the conversion factor. Our results for the numerical cross section can be found in Fig. 8. Despite the difference in the amplitude plots, the analytic and numerical cross sections agree very well as can be seen in the figure. The numerical to

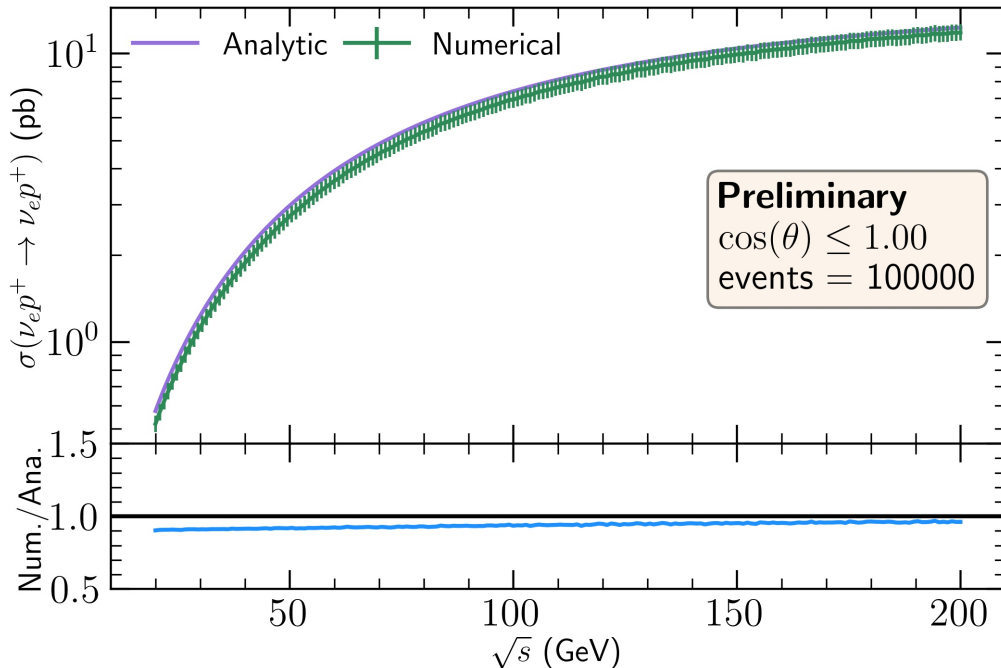


**Figure 8.** Cross section  $\sigma$  for the process  $\nu_e p^+ \rightarrow \nu_e p^+$  as a function of the center-of-mass energies  $E_{CM} = \sqrt{s}$ . For each of the 190 evenly spaced values of  $E_{CM}$ , we calculated  $\frac{1}{2} \sum |\mathcal{M}|^2$  with  $10^5$  events.

analytic ratio starts at about 0.9 at low energies and grows closer to 1 at higher energies. This agreement is not surprising given that the discrepancy mentioned earlier was caused due to a missing normalization factor. This concludes our analysis of the  $\nu_e p^+ \rightarrow \nu_e p^+$  process.

### 3.3 Preliminary Results

In this section, we will cover the latest preliminary results of our program. These new plots will be based on the leptonic tensor approach that takes into account the nuclear physics effects of the interaction with hadrons, and that relies on the multichannel and VEGAS techniques from Sec. 2.3 and Sec. 2.4. Our program, based on the Comix matrix element generator from Sherpa, was used to calculate the leptonic tensor.

For this section, we have simulated the scattering of an electron off a carbon-12 nucleus,

$$e^- + {}^{12}\text{C} \rightarrow e^- + p^+ + X, \quad (3.9)$$

where  $X$  is an unknown nucleus that remains from our interaction with carbon. The theoretical expression of the hadronic tensor for our program’s results is based on Ref. [29], and the computational implementation is based on private communication with Dr. Rocco. This implementation of  $H^{\mu\nu}$  is currently tailored to carbon-12.

In Fig. 9, we have the differential cross section with respect to the outgoing lepton energy of our process,  $\frac{d\sigma}{dE_l}$  expressed in units of  $\text{mb MeV}^{-1}$ . As we can see, both approaches

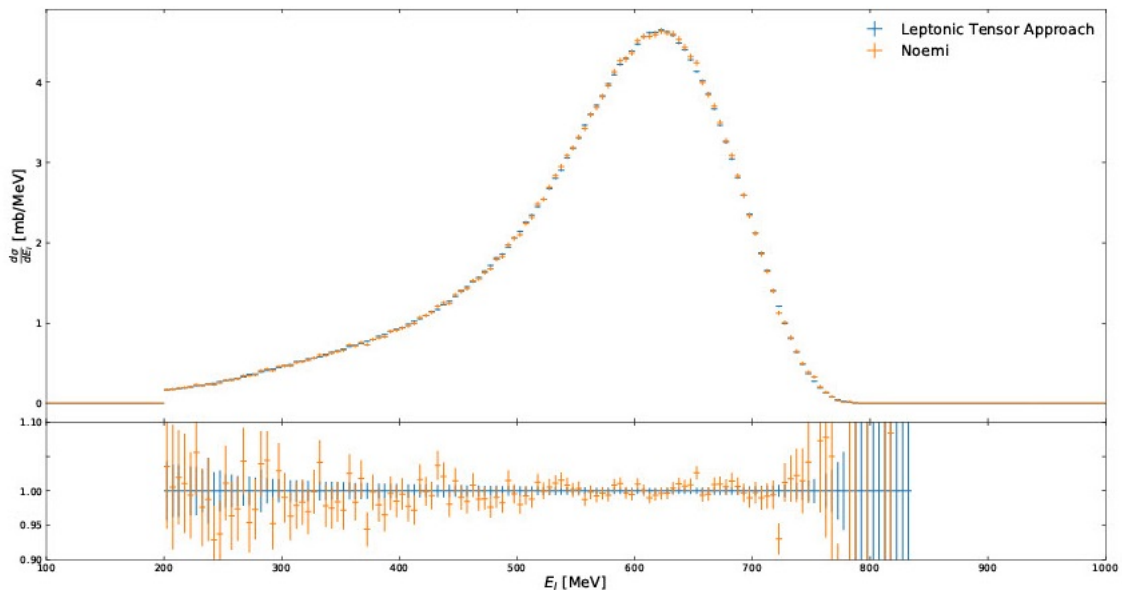


**Figure 9.** Differential cross section [mb MeV<sup>-1</sup>] of  $e^- {}^{12}\text{C} \rightarrow e^- p^+ X$  with respect to the outgoing energy of the lepton [MeV] ( $e^-$ ). In blue, we have the results from our new leptonic tensor approach and in orange, we have the results from Dr. Rocco’s program based on Ref. [29]. The bottom panel shows the results of each approach normalized to unity for comparison.

agree very well throughout the whole energy range from 200 to  $\sim 850$  MeV. This agreement can be further seen in the bottom panel of Fig. 9, where we have plotted the ratio to the leptonic tensor approach for comparison and the results agree within the uncertainties.

In Fig. 10, we have the differential cross section with respect to the cosine of the outgoing lepton angle of our process,  $\frac{d\sigma}{d\cos\theta}$  expressed in units of mb. As we can see, both approaches agree very well throughout the range  $[-1, 1]$ . This agreement can be further seen in the bottom panel of Fig. 10, where we have plotted the ratio to the leptonic tensor approach for comparison and the results agree within the uncertainties.

Finally, in Fig. 11, we have the differential cross section with respect to the momentum of the outgoing hadron ( $p^+$ ),  $\frac{d\sigma}{dp_H}$  expressed in units of mb MeV<sup>-1</sup>. As we can see, both approaches agree very well throughout the range  $[10, 1000]$  MeV. This agreement can be further seen in the bottom panel of Fig. 11, where we have plotted the ratio to the leptonic tensor approach for comparison and the results agree within the uncertainties.

## 4 Conclusion and Future Steps

We live in an exciting time for particle physics, particularly for neutrino physics. Within the coming decades, two experiments, the Deep Underground Neutrino Experiment (DUNE) and Tokai-to-Hyper-Kamiokande (T2HK), will provide us with unprecedented data of neutrino events that will hopefully hold the key to new physical phenomena unexplained by the Standard Model (SM). With this colossal amount of data available, physicists will require a fast and efficient method of testing the myriad of Beyond the Standard Model (BSM)

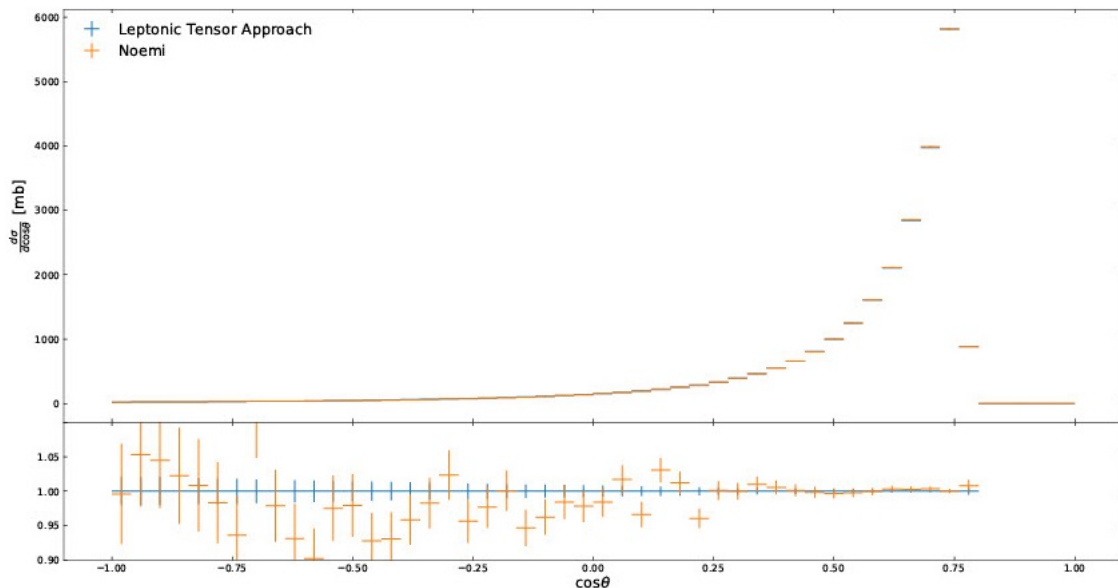


**Figure 10.** Differential cross section [mb] of  $e^- {}^{12}\text{C} \rightarrow e^- p^+ X$  with respect to the cosine of the outgoing angle of the lepton ( $e^-$ ) with respect to the beam axis. In blue, we have the results from our new leptonic tensor approach and in orange, we have the results from Dr. Rocco’s program based on Ref. [29]. The bottom panel shows the results of each approach normalized to unity for comparison.

theories. For this project, we proposed an algorithm capable of achieving this by automatically calculating the leptonic tensor of given processes. For the development of our algorithm, we utilized the `Universal FeynRules Output (UFO)` [15] file format to obtain the relevant information of the theory, and the Berends-Giele recursive relations [11] for proper parsing and computation of the leptonic tensors. Our algorithm relies on the `Comix` matrix element generator from `Sherpa`. To test our program, we computed the numerical squared amplitudes and cross sections of two SM processes:  $e^- p^+ \rightarrow e^- p^+$  and  $\nu_e p^+ \rightarrow \nu_e p^+$ . Both of these processes showed excellent agreement with analytic results. We were also able to show some preliminary results of our program for the process  $e^- {}^{12}\text{C} \rightarrow e^- p^+ X$  that takes into account the nuclear effects in the hadronic tensor and that utilizes the multichannel Monte Carlo phase space integration approach and the `VEGAS` technique to estimate the differential cross sections. The results were promising, showing an excellent agreement when compared to Dr. Rocco’s calculations. This agreement validates our new leptonic tensor approach, and will allow us to test more complicated processes with the confidence that we are producing the correct results. For the future, we hope to obtain more plots from the current version of the algorithm that we plan to test with more complicated SM events such as the neutrino trident process  $\nu_\mu N \rightarrow \nu_\mu N \mu^+ \mu^-$  as well as with BSM theories.

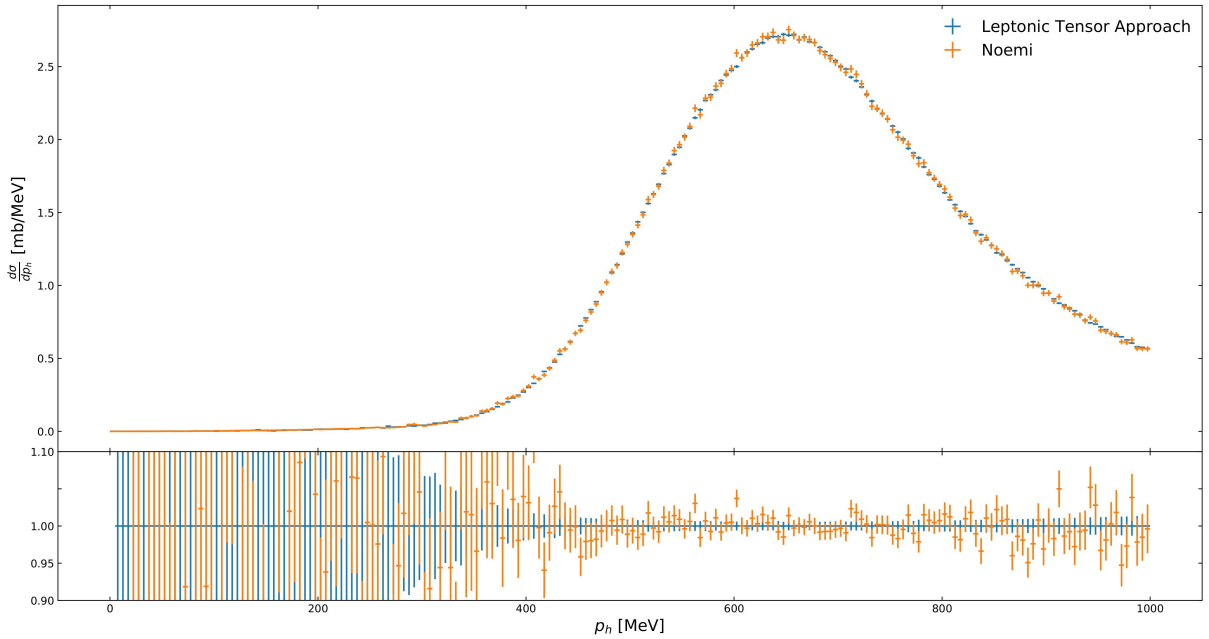


**Figure 11.** Differential cross section [mb MeV<sup>-1</sup>] of  $e^-^{12}\text{C} \rightarrow e^-p^+X$  with respect to the momentum of the outgoing hadron ( $p^+$ ). In blue, we have the results from our new leptonic tensor approach and in orange, we have the results from Dr. Rocco’s program based on Ref. [29]. The bottom panel shows the results of each approach normalized to unity for comparison.

## Acknowledgments

This manuscript has been authored by Fermi Research Alliance, LLC under Contract No. DE-AC02-07CH11359 with the U.S. Department of Energy, Office of Science, Office of High Energy Physics.

## References

- [1] K. Abe et al. Physics potential of a long-baseline neutrino oscillation experiment using a J-PARC neutrino beam and Hyper-Kamiokande. *PTEP*, 2015:053C02, 2015.
- [2] P. Abratenko, C. Adams, M. Alrashed, R. An, J. Anthony, J. Asaadi, A. Ashkenazi, M. Auger, S. Balasubramanian, B. Baller, C. Barnes, G. Barr, M. Bass, F. Bay, A. Bhat, K. Bhattacharya, M. Bishai, A. Blake, T. Bolton, L. Camilleri, D. Caratelli, I. Caro Terrazas, R. Carr, R. Castillo Fernandez, F. Cavanna, G. Cerati, Y. Chen, E. Church, D. Cianci, E. O. Cohen, G. H. Collin, J. M. Conrad, M. Convery, L. Cooper-Troendle, J. I. Crespo-Anad3n, M. Del Tutto, D. Devitt, A. Diaz, L. Domine, K. Duffy, S. Dytman, B. Eberly, A. Ereditato, L. Escudero Sanchez, J. Esquivel, J. J. Evans, R. S. Fitzpatrick, B. T. Fleming, D. Franco, A. P. Furmanski, D. Garcia-Gamez, V. Genty, D. Goeldi, S. Gollapinni, O. Goodwin, E. Gramellini, H. Greenlee, R. Grosso, L. Gu, W. Gu, R. Guenette, P. Guzowski, A. Hackenburg, P. Hamilton, O. Hen, C. Hill, G. A. Horton-Smith, A. Hourlier, E.-C. Huang, C. James, J. Jan de Vries, X. Ji, L. Jiang, R. A.

- Johnson, J. Joshi, H. Jostlein, Y.-J. Jwa, G. Karagiorgi, W. Ketchum, B. Kirby, M. Kirby, T. Kobilarcik, I. Kreslo, I. Lepetic, Y. Li, A. Lister, B. R. Littlejohn, S. Lockwitz, D. Lorca, W. C. Louis, M. Luethi, B. Lundberg, X. Luo, A. Marchionni, S. Marocco, C. Mariani, J. Marshall, J. Martin-Albo, D. A. Martinez Caicedo, K. Mason, A. Mastbaum, V. Meddage, T. Mettler, J. Mills, K. Mistry, A. Mogan, J. Moon, M. Mooney, C. D. Moore, J. Mousseau, M. Murphy, R. Murrells, D. Naples, P. Nienaber, J. Nowak, O. Palamara, V. Pandey, V. Paolone, A. Papadopoulou, V. Papavassiliou, S. F. Pate, Z. Pavlovic, E. Piasetzky, D. Porzio, G. Pulliam, X. Qian, J. L. Raaf, A. Rafique, L. Ren, L. Rochester, H. E. Rogers, M. Ross-Lonergan, C. Rudolf von Rohr, B. Russell, G. Scanavini, D. W. Schmitz, A. Schukraft, W. Seligman, M. H. Shaevitz, R. Sharankova, J. Sinclair, A. Smith, E. L. Snider, M. Soderberg, S. Söldner-Rembold, S. R. Soleti, P. Spentzouris, J. Spitz, M. Stancari, J. St. John, T. Strauss, K. Sutton, S. Sword-Fehlberg, A. M. Szelc, N. Tagg, W. Tang, K. Terao, M. Thomson, R. T. Thornton, M. Touns, Y.-T. Tsai, S. Tufanli, T. Usher, W. Van De Pontseele, R. G. Van de Water, B. Viren, M. Weber, H. Wei, D. A. Wickremasinghe, K. Wierman, Z. Williams, S. Wolbers, T. Wongjirad, K. Woodruff, W. Wu, T. Yang, G. Yarbrough, L. E. Yates, G. P. Zeller, J. Zennamo, and C. Zhang. First Measurement of Inclusive Muon Neutrino Charged Current Differential Cross Sections on Argon at  $E_\nu \sim 0.8$  GeV with the MicroBooNE Detector. *Phys. Rev. Lett.*, 123:131801, Sep 2019.
- [3] R. Acciarri et al. Long-Baseline Neutrino Facility (LBNF) and Deep Underground Neutrino Experiment (DUNE): Conceptual Design Report, Volume 2: The Physics Program for DUNE at LBNF. 12 2015.
- [4] Mario A. Acero, Carlo Giunti, and Marco Laveder. Limits on  $\nu_e$  and  $\bar{\nu}_e$  disappearance from Gallium and reactor experiments. *Phys. Rev. D*, 78:073009, Oct 2008.
- [5] A. Aguilar, L. B. Auerbach, R. L. Burman, D. O. Caldwell, E. D. Church, A. K. Cochran, J. B. Donahue, A. Fazely, G. T. Garvey, R. M. Gunasingha, R. Imlay, W. C. Louis, R. Majkic, A. Malik, W. Metcalf, G. B. Mills, V. Sandberg, D. Smith, I. Stancu, M. Sung, R. Tayloe, G. J. VanDalen, W. Vernon, N. Wadia, D. H. White, and S. Yellin. Evidence for neutrino oscillations from the observation of  $\bar{\nu}_e$  appearance in a  $\bar{\nu}_\mu$  beam. *Phys. Rev. D*, 64:112007, Nov 2001.
- [6] A. A. Aguilar-Arevalo, C. E. Anderson, S. J. Brice, B. C. Brown, L. Bugel, J. M. Conrad, R. Dharmapalan, Z. Djurcic, B. T. Fleming, R. Ford, F. G. Garcia, G. T. Garvey, J. Mirabal, J. Grange, J. A. Green, R. Imlay, R. A. Johnson, G. Karagiorgi, T. Katori, T. Kobilarcik, S. K. Linden, W. C. Louis, K. B. M. Mahn, W. Marsh, C. Mauger, W. Metcalf, G. B. Mills, C. D. Moore, J. Mousseau, R. H. Nelson, V. Nguyen, P. Nienaber, J. A. Nowak, B. Osmanov, Z. Pavlovic, D. Perevalov, C. C. Polly, H. Ray, B. P. Roe, A. D. Russell, R. Schirato, M. H. Shaevitz, M. Sorel, J. Spitz, I. Stancu, R. J. Stefanski, R. Tayloe, M. Tzanov, R. G. Van de Water, M. O. Wascko, D. H. White, M. J. Wilking, G. P. Zeller, and E. D. Zimmerman. Event Excess in the MiniBooNE Search for  $\bar{\nu}_\mu \rightarrow \bar{\nu}_e$  Oscillations. *Phys. Rev. Lett.*, 105:181801, Oct 2010.
- [7] A. A. Aguilar-Arevalo, B. C. Brown, L. Bugel, G. Cheng, J. M. Conrad, R. L. Cooper, R. Dharmapalan, A. Diaz, Z. Djurcic, D. A. Finley, R. Ford, F. G. Garcia, G. T. Garvey, J. Grange, E.-C. Huang, W. Huelsnitz, C. Ignarra, R. A. Johnson, G. Karagiorgi, T. Katori, T. Kobilarcik, W. C. Louis, C. Mariani, W. Marsh, G. B. Mills, J. Mirabal, J. Monroe, C. D. Moore, J. Mousseau, P. Nienaber, J. Nowak, B. Osmanov, Z. Pavlovic, D. Perevalov, H. Ray, B. P. Roe, A. D. Russell, M. H. Shaevitz, J. Spitz, I. Stancu, R. Tayloe, R. T. Thornton, M. Tzanov, R. G. Van de Water, D. H. White, D. A. Wickremasinghe, and E. D.

- Zimmerman. Significant Excess of Electronlike Events in the MiniBooNE Short-Baseline Neutrino Experiment. Phys. Rev. Lett., 121:221801, Nov 2018.
- [8] Q.R. Ahmad et al. Direct evidence for neutrino flavor transformation from neutral current interactions in the Sudbury Neutrino Observatory. Phys. Rev. Lett., 89:011301, 2002.
- [9] Adam Alloul, Neil D. Christensen, Céline Degrande, Claude Duhr, and Benjamin Fuks. Feynrules 2.0 a complete toolbox for tree-level phenomenology. Computer Physics Communications, 185(8):2250–2300, 2014.
- [10] C. Andreopoulos et al. The GENIE Neutrino Monte Carlo Generator. Nucl. Instrum. Meth. A, 614:87–104, 2010.
- [11] Frits A. Berends and W.T. Giele. Recursive Calculations for Processes with  $n$  Gluons. Nucl. Phys. B, 306:759–808, 1988.
- [12] Enrico Bertuzzo, Sudip Jana, Pedro A. N. Machado, and Renata Zukanovich Funchal. Dark neutrino portal to explain miniboone excess. Phys. Rev. Lett., 121:241801, Dec 2018.
- [13] O. Buss, T. Gaitanos, K. Gallmeister, H. van Hees, M. Kaskulov, O. Lalakulich, A. B. Larionov, T. Leitner, J. Weil, and U. Mosel. Transport-theoretical Description of Nuclear Reactions. Phys. Rept., 512:1–124, 2012.
- [14] Neil D. Christensen and Claude Duhr. FeynRules - Feynman rules made easy. Comput. Phys. Commun., 180:1614–1641, 2009.
- [15] Celine Degrande, Claude Duhr, Benjamin Fuks, David Grellscheid, Olivier Mattelaer, and Thomas Reiter. UFO - The Universal FeynRules Output. Comput. Phys. Commun., 183:1201–1214, 2012.
- [16] Mona Dentler, Álvaro Hernández-Cabezudo, Joachim Kopp, Michele Maltoni, and Thomas Schwetz. Sterile neutrinos or flux uncertainties? — Status of the reactor anti-neutrino anomaly. JHEP, 11:099, 2017.
- [17] K. Eguchi et al. First results from KamLAND: Evidence for reactor anti-neutrino disappearance. Phys. Rev. Lett., 90:021802, 2003.
- [18] Y. Fukuda et al. Measurement of the flux and zenith angle distribution of upward through going muons by Super-Kamiokande. Phys. Rev. Lett., 82:2644–2648, 1999.
- [19] Carlo Giunti and Marco Laveder. Statistical significance of the gallium anomaly. Phys. Rev. C, 83:065504, Jun 2011.
- [20] Tanju Gleisberg and Stefan Hoeche. Comix, a new matrix element generator. JHEP, 12:039, 2008.
- [21] Tomasz Golan, Cezary Juszczak, and Jan T. Sobczyk. Final State Interactions Effects in Neutrino-Nucleus Interactions. Phys. Rev., C86:015505, 2012.
- [22] Y. Hayato. NEUT. Nucl. Phys. B Proc. Suppl., 112:171–176, 2002.
- [23] Stefan Höche, Silvan Kuttimalai, Steffen Schumann, and Frank Siegert. Beyond Standard Model calculations with Sherpa. Eur. Phys. J. C, 75(3):135, 2015.
- [24] R Kleiss, W.J Stirling, and S.D Ellis. A new monte carlo treatment of multiparticle phase space at high energies. Computer Physics Communications, 40(2):359–373, 1986.
- [25] Ronald Kleiss and Roberto Pittau. Weight optimization in multichannel monte carlo. Computer Physics Communications, 83(2):141–146, 1994.

- [26] G. Mention, M. Fechner, Th. Lasserre, Th. A. Mueller, D. Lhuillier, M. Cribier, and A. Letourneau. Reactor antineutrino anomaly. Phys. Rev. D, 83:073006, Apr 2011.
- [27] Ulrich Mosel. Neutrino event generators: foundation, status and future. J. Phys. G, 46(11):113001, 2019.
- [28] G Peter Lepage. A new algorithm for adaptive multidimensional integration. Journal of Computational Physics, 27(2):192–203, 1978.
- [29] Noemi Rocco. Ab initio calculations of lepton-nucleus scattering. Frontiers in Physics, 8:116, 2020.